

# Gallium Plasmonic Nanoantennas Unveiling Multiple Kinetics of Hydrogen Sensing, Storage, and Spillover

Maria Losurdo,\* Yael Gutiérrez, Alexandra Suvorova, Maria M. Giangregorio, Sergey Rubanov, April S. Brown, and Fernando Moreno

Hydrogen is the key element to accomplish a carbon-free based economy. Here, the first evidence of plasmonic gallium (Ga) nanoantennas is provided as nanoreactors supported on sapphire ( $\alpha\text{-Al}_2\text{O}_3$ ) acting as direct plasmon-enhanced photocatalyst for hydrogen sensing, storage, and spillover. The role of plasmon-catalyzed electron transfer between hydrogen and plasmonic Ga nanoparticle in the activation of those processes is highlighted, as opposed to conventional refractive index-change-based sensing. This study reveals that, while temperature selectively operates those various processes, longitudinal (LO-LSPR) and transverse (TO-LSPR) localized surface plasmon resonances of supported Ga nanoparticles open selectivity of localized reaction pathways at specific sites corresponding to the electromagnetic hot-spots. Specifically, the TO-LSPR couples light into the surface dissociative adsorption of hydrogen and formation of hydrides, whereas the LO-LSPR activates heterogeneous reactions at the interface with the support, that is, hydrogen spillover into  $\alpha\text{-Al}_2\text{O}_3$  and reverse-oxygen spillover from  $\alpha\text{-Al}_2\text{O}_3$ . This Ga-based plasmon-catalytic platform expands the application of supported plasmon-catalysis to hydrogen technologies, including reversible fast hydrogen sensing in a timescale of a few seconds with a limit of detection as low as 5 ppm and in a broad temperature range from room-temperature up to 600 °C while remaining stable and reusable over an extended period of time.

hydrogen sensing and storage new materials solutions are needed to reduce thermodynamic (process-temperatures limitations) and kinetic (process rate limitations) barriers and meet the challenges of sensing of a response time of less than 1 s, an operating temperature of  $-30$  to  $80$  degrees Celsius, and a measurement of 0.1% to 10%,<sup>[1]</sup> as well as of hydrogen storage with low hydrogen refilling time and output power.

The integration of plasmonics<sup>[2]</sup> with the recently introduced concept of novel catalytically-active liquid metal hydrides and hydrogen trapping mechanisms represents a breakthrough toward creating a new generation of plasmonic-enhanced photocatalytic nanosystems for enhancing both hydrogen sensing<sup>[3]</sup> and storage.<sup>[4]</sup>

Surface-plasmon-resonance (SPR) induces electromagnetic field enhancement on common hydrogen-absorbing metals such as magnesium (Mg), palladium (Pd), titanium (Ti), and nickel (Ni) which may be exploitable in the microwave region for hydrogen storage.<sup>[5,6]</sup>


Previous studies have reported SPR hydrogen sensing platforms based on Pd,<sup>[7,8]</sup> gold (Au),<sup>[9–11]</sup> aluminum (Al),<sup>[12]</sup> and Mg<sup>[13]</sup> nanoparticles (NPs). Considering the essential requirements for hydrogen storage, such as high storage capacity and fast hydrogen adsorption kinetics, requirements of hydrogen

## 1. Introduction

One of the most interesting applications of nanotechnology is the use of sunlight-driven chemical activity at the nanoscale to accomplish a carbon-free, hydrogen economy. For both

Dr. M. Losurdo, Dr. Y. Gutiérrez, Dr. M. M. Giangregorio  
 Institute of Nanotechnology  
 CNR-NANOTEC  
 via Orabona 4, Bari 70126, Italy  
 E-mail: maria.losurdo@cnt.it

Dr. A. Suvorova  
 Centre for Microscopy  
 Characterisation and Analysis  
 The University of Western Australia  
 Crawley, Western Australia 6009, Australia

 The ORCID identification number(s) for the author(s) of this article can be found under <https://doi.org/10.1002/adma.202100500>.

© 2021 The Authors. Advanced Materials published by Wiley-VCH GmbH. This is an open access article under the terms of the Creative Commons Attribution-NonCommercial License, which permits use, distribution and reproduction in any medium, provided the original work is properly cited and is not used for commercial purposes.

DOI: 10.1002/adma.202100500

Prof. S. Rubanov  
 Bio21 Institute  
 University of Melbourne  
 161 Barry Street, Parkville, Victoria 3010, Australia  
 Prof. A. S. Brown  
 Department of Electrical and Computer Engineering  
 Duke University  
 Durham, NC 27708, USA  
 Prof. F. Moreno  
 Group of Optics, Department of Applied Physics  
 Faculty of Sciences  
 University of Cantabria  
 Avda. Los Castros s/n, Santander 39005, Spain

adsorption/desorption with fast response time and large dynamic operational range, and requirements for sensing, high detection sensitivity, and good cyclability, each of the above metals have limitations. Mg suffers from the high-temperatures (650–700 K)<sup>[14]</sup> required to desorb hydrogen and, consequently, a slow desorption kinetics.<sup>[15]</sup> Pd is a poor plasmonic metal with low extinction and scattering cross-sections responsible for its low sensitivity;<sup>[16]</sup> furthermore, the lattice undergoes hydrogen embrittlement associated with the  $\alpha$ - to  $\beta$ -phase transition which limits the hydrogen cycling and reversibility, causing hysteresis in the loading and unloading of hydrogen and, consequently, a nonlinear behavior of the sensor response.<sup>[8]</sup> Au NPs are not CMOS-compatible, which limits their feasibility in low-cost and large-scale applications. Al NPs are efficient plasmonic nanoantennas but suffer from metastability of aluminum hydride (AlH<sub>3</sub>) that is a crystalline solid at room temperature with difficult regeneration after hydrogen desorption.<sup>[17]</sup> Indirect plasmonic hydrogen sensing based on the Pd–Al<sup>[18]</sup> and Pd–Au<sup>[19]</sup> combination has been proposed where Pd is the hydrogen reacting element, while Al or Au is the plasmonic antenna enhancing the Pd changes upon interaction with hydrogen; this indirect sensing requires double nanolithography steps to control the nanostructuring of the two metals.

All this motivates continuous efforts to develop new materials, for example, metallic alloys, and new approaches, for example, nanostructuring, doping, and plasmonic-photocatalysis, to improve hydrogen sensing and storage.

In the last years, we have demonstrated that gallium (Ga) NPs are plasmonically tunable over a wide spectral range, that is, they show localized surface plasmon resonance (LSPR) modes from ultraviolet (UV) to the visible, and to the near infrared (NIR),<sup>[20–22]</sup> and are stable over a broad temperature range up to 600 °C,<sup>[20]</sup> enabling high temperature measurements and applications overcoming restrictions for many endothermic reactions or reactions with slow kinetics. Furthermore, as opposed to all the previous reported metals, Ga is a liquid metal that, differently from Pd, can expand with hydrogen incorporation avoiding metal embrittlement.

Intriguingly, very recently, *ab initio* density functional theory calculations have indicated a high potential<sup>[23–25]</sup> of Ga in hydrogen technologies because Ga can dissociate H<sub>2</sub> at such reduced temperatures by charge transfer processes,<sup>[24]</sup> and Ga clusters decorated with specific metals are characterized by a low H<sub>2</sub> adsorption energy  $E_{\text{ads}}$  of 0.30–0.58 eV, thereby allowing storage and desorption cycling at near-ambient conditions.<sup>[25]</sup>

Here, we report, for the first time to the best of our knowledge, the discovery that plasmonic Ga NPs on a sapphire ( $\alpha$ -Al<sub>2</sub>O<sub>3</sub>) support function as direct nanoantennas for several plasmonic photocatalyzed interactions with hydrogen, discerning their different regimes of temperature ( $T$ ), that is:

- i. Plasmon-enhanced hydrogen sensing at  $T < 200$  °C, with an almost null activation energy for the hydrogen adsorption;
- ii. Hydrogen storage in the form of interstitial hydrogen and metallic hydrides at  $200$  °C  $< T < 600$  °C;
- iii. Hydrogen spillover and reverse-oxygen spillover<sup>[26]</sup> involving the  $\alpha$ -Al<sub>2</sub>O<sub>3</sub> support at  $T > 600$  °C, mostly localized at the longitudinal Ga NPs hot-spots.

Therefore, operative parameters can be inferred as guidance to design the Ga plasmonic-catalysts nanoreactors depending on the hydrogen process to be activated.

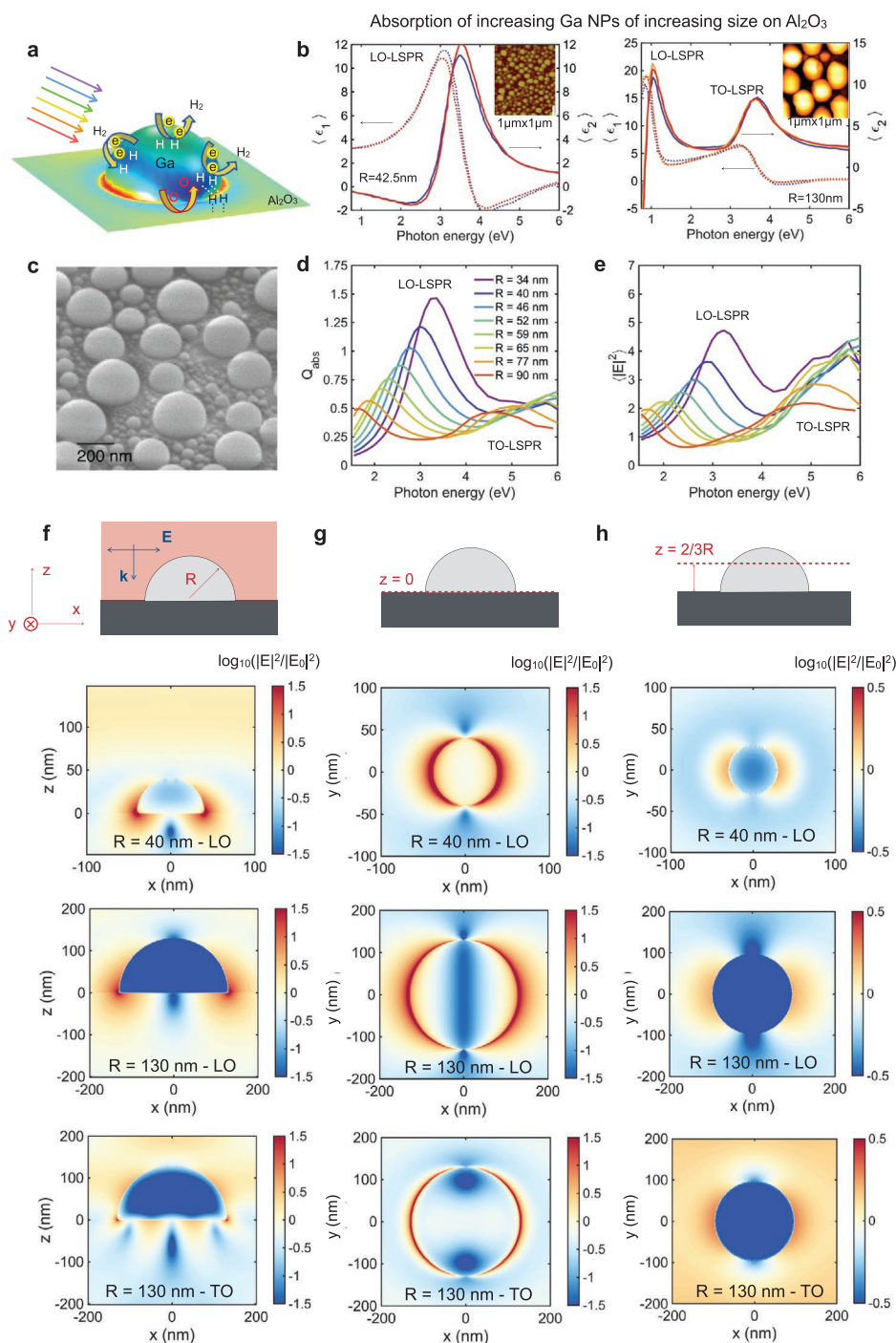
## 2. Results and Discussion

### 2.1. The Ga NPs Longitudinal and Transverse Plasmonic Hot Spots

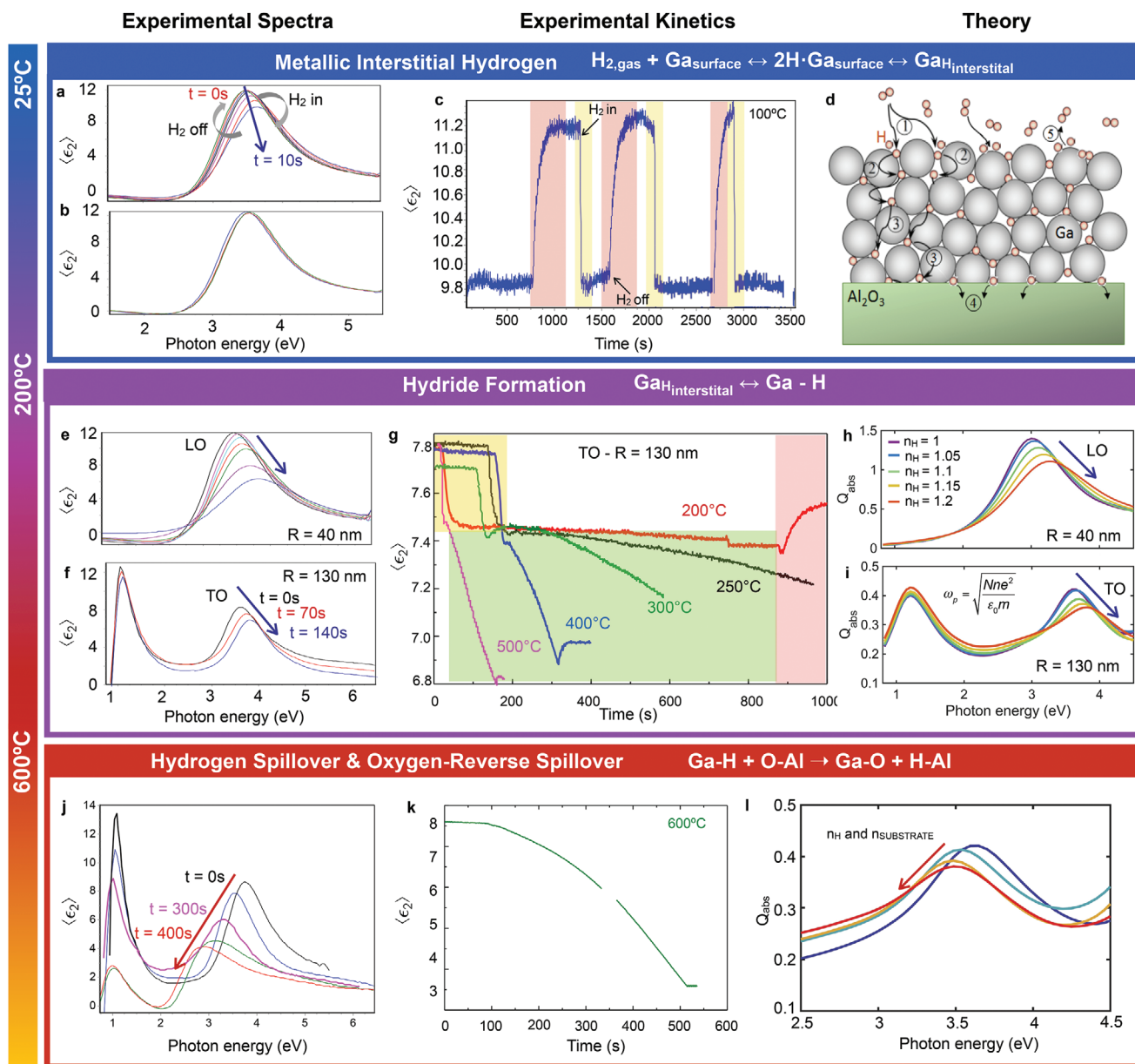
In order to gain better insight and understanding of the interaction with hydrogen and its dependence on the NPs geometry, we first design and analyze the optical response of the Ga NPs sensor/nanoreactor.

Figure 1 shows the characteristics and advantages of the Ga NPs plasmonic platform, such as the easy self-assembly of well-shaped hemispherical NPs without the use of lithography. The NP shape is controlled by the interface energies, resulting in reproducible LSPR from run to run simply controlling the deposited Ga amount (Figure 1c).<sup>[20]</sup> The experimental plasmonic response of selected samples measured through spectroscopic ellipsometry is shown in Figure 1b. Among the fabricated samples of Ga NPs with different size ranging from diameter of 50 nm up to 400 nm, we select a set of hemispherical Ga NPs with an average diameter  $D = 260 \pm 10$  nm and height  $h = 150 \pm 5$  nm, with a measured longitudinal localized surface plasmon resonance (LO-LSPR) at  $1.05 \pm 0.05$  eV and transverse localized surface plasmon resonance (TO-LSPR) at  $3.55 \pm 0.05$  eV, and a second set with  $D = 85 \pm 5$  nm and  $h = 40 \pm 1$  nm whose LO-LSPR is at  $3.55 \pm 0.05$  eV and TO-LSPR occurs at an energy higher than 6.5 eV. Those samples provide either the TO or LO LSPR at the same energy (3.55 eV) that allows to investigate, independently of the energy/wavelength, how the different spatial distribution of the longitudinal and transverse electromagnetic near-field enhancements and associated hot-spots affect the interaction with hydrogen.

Those experimental spectra well agree with the numerical simulations of the absorption cross-section of non-interacting<sup>[27]</sup> Ga NPs of increasing radius supported on a sapphire substrate as in Figure 1d, which shows the unique characteristic of the supported Ga NPs, that is, the large spectral separation between the longer wavelength/lower energy longitudinal plasmon mode (LO-LSPR) and shorter wavelength/higher energy transverse plasmon mode (TO-LSPR), both modes tunable from the UV to NIR by increasing NPs radius. Figure 1e shows the near-field enhancement averaged over the NP surface ( $\langle |E|^2 \rangle$ ), revealing that both LO and TO have a similar value of  $\langle |E|^2 \rangle$  for the smallest NPs. As the size increases, the value for TO mode surpasses that corresponding to the LO mode. A general trend observed is the decrease of  $\langle |E|^2 \rangle$  with the increase of the NP size. Importantly, although the LO and TO may present a similar value of the near-field enhancement averaged over the surface, their near-field ( $|E|^2$ ) spatial distribution and hot-spots are quite different, as shown by the electromagnetic field enhancement maps in Figures 1f–h. These maps are plotted in a plane perpendicular to the substrate that contains the propagation direction ( $\mathbf{k}$ ) and electric field polarization vector ( $\mathbf{E}_0$ ) of the incident beam (Figure 1f, side view) and in two planes at different height parallel to the substrate, that is, at the substrate



**Figure 1.** Plasmonic Ga antenna–hydrogen reactor system. a) Scheme of a Ga nanoparticle working as a plasmonic antenna and through localized near-field enhancements also as a photocatalytic nanoreactor for hydrogen dissociation, storage, and hydrogen spillover as well as oxygen-reverse spillover. b) Experimental spectra of the real, ( $\epsilon_1$ ), and imaginary, ( $\epsilon_2$ ), parts of the pseudodielectric function measured by spectroscopic ellipsometry showing the absorption of the Ga NPs ensemble and specifically the LO- (electric field parallel to the support surface) LSPR mode and the TO- (electric field perpendicular to the support surface) LSPR modes of Ga NPs with an average diameter of 85 and 260 nm with their corresponding AFM images shown as the inset. The three curves for the 260 nm sample and the two curves for the 85 nm sample are for samples deposited in different days to show the good reproducibility and control of the LSPR by the Ga NPs size. c) SEM tilted view showing the random isotropic distribution of the self-assembled Ga NPs on  $\alpha\text{-Al}_2\text{O}_3$  support, to better show their hemispherical shape. d) Calculated absorption efficiency spectra as a function of the radius,  $R$ , of the Ga hemisphere on a  $\text{Al}_2\text{O}_3$  substrate illuminated at normal incidence showing the tunability of the LO- and TO-LSPR modes. e) Near-field enhancement averaged ( $\langle |E|^2 \rangle$ ) over the surface of Ga hemispheres with same  $R$  as in (d). f–h) Near-field enhancement maps plotted in the plane containing the incident beam wave vector ( $\mathbf{k}$ ) and electric field polarization vector ( $\mathbf{E}_0$ ) (f), and in planes parallel to the substrate at  $z = 0$  (interface with the substrate) (g) and at  $z = 2R/3$  (h). Those maps are shown for the LO-LSPR of Ga NPs with  $R = 85$  nm, and for the LO-LSPR and TO-LSPR of Ga NPs with  $R = 130$  nm on a  $\text{Al}_2\text{O}_3$  substrate.



**Figure 2.** Kinetics and spectral variation of LSPR of Ga NPs during exposure to hydrogen. a,b,e,f,i,j) Time evolution of experimental  $\langle \epsilon_2 \rangle$  spectra (each spectrum every 1 s) showing the evolution of the plasmon resonance during exposure of the Ga NPs to 1 Torr of hydrogen at temperatures of 100 °C (a,b): (a) is showing the change during one cycle of hydrogen in and out; (b) shows the initial spectrum (blue line), the final spectrum after first cycle of hydrogen in-out (green line) and after second cycle of hydrogen in-out (red line); 200 °C (e,f) and 600 °C (j). c,g,k) Experimental kinetics of the variation of the maximum of the plasmon resonance monitored by recording the imaginary part of the pseudodielectric function,  $\langle \epsilon_2 \rangle$ , in real time every 1 s at LSPR maximum during exposure of the Ga NPs to 1 Torr of hydrogen at temperatures of 100 °C (c), 200–500 °C (g), and 600 °C (k). In (g) the yellow shadowed area indicates the interstitial diffusion; the green area indicates the reactive step of Ga–H bond formation; the red area indicates the desorption step. d) Scheme of the possible dissociative adsorption of hydrogen at: 1) the Ga NP surface, 2) its interstitial diffusion into the Ga NPs, 4) the reactive step to hydride Ga–H, the spillover reaction at the interface with  $\text{Al}_2\text{O}_3$ , and 5) the associative desorption, according to reactions (1–4) described in the main text. h,i) Calculated absorption efficiency,  $Q_{\text{abs}}$ , for  $R = 40$  nm (h) and  $R = 130$  nm (i) Ga hemispherical NPs on a  $\text{Al}_2\text{O}_3$  substrate as the electronic density,  $n_{\text{H}}$ , inside the metal NPs increases simulating the metallic interstitial hydrogen (see Section S1, Supporting Information for details). f) Calculated absorption efficiency of an  $R = 130$  nm Ga hemispherical NP on a  $\text{Al}_2\text{O}_3$  substrate as the refractive index of the interface with the substrate and that of the surrounding medium increase,  $n_{\text{substrate}}$ , simulating the formation of the  $\text{Ga}_2\text{O}_3$  (see Section S2, Supporting Information for details). All measurements have been performed under broadband illumination from a xenon lamp. The arrows in (a,e,f,i,j) represent the increase of exposure time to hydrogen and some of the times have been specified. The arrows in (h,i,l) indicate the increase of the electron density in the Ga NPs according to the colors specified in the legend.

surface (Figure 1g,  $z = 0$ , top view), and at  $z = 2R/3$  (Figure 1h, top view). It is worth noting that  $|\mathbf{E}|^2$  is plotted in logarithmic scale. Specifically, the LO-mode hot-spots are localized at the

Ga-NP/ $\text{Al}_2\text{O}_3$ -substrate interface; the comparison of the  $|\mathbf{E}|^2$  scale for the 40 nm NPs at  $z = 0$  (Figure 1g) and at  $z = 2R/3$  (Figure 1h) clearly shows a much intense  $|\mathbf{E}|^2$  at the interface



with the substrate. The LO resonance is purely dipolar, and the electron plasma oscillates with the largest amplitude along the hemisphere diameter, parallel to the interface Ga-NP/Al<sub>2</sub>O<sub>3</sub>-substrate interface. TO-mode hot-spots are distributed over the surface of the Ga hemisphere (e.g., compare  $|E|^2$  maps in Figure 1h for  $z = 2R/3$ ) and are more prone to promote the hydrogen dissociative adsorption on the Ga NPs surface and sense it. This different spatial distribution is relevant to identify different reaction sites where the hydrogen-Ga NPs interaction senses a different electromagnetic field.

The electronic and chemical interaction of Ga NPs with hydrogen is a complex function of the electromagnetic enhancement (i.e., plasmonic mode) as well as of the temperature. Therefore, **Figure 2** shows the variation of LO-LSPR and TO-LSPR spectra as a function of time exposure to hydrogen and the corresponding kinetic profile at the LSPR maxima for various temperatures in the range 25–600 °C, being 600 °C the high temperature where those Ga NPs have been demonstrated to be thermally stable<sup>[20]</sup> (in absence of hydrogen). Differently from the usual a redshift of LSPR observed during sensing<sup>[28]</sup> (see also Section S3, Supporting Information for the present Ga NPs), the spectral and kinetic data in Figure 2 show new phenomena associated with the Ga LO- and TO-LSPR upon exposure to hydrogen:

- i. A reversible blueshift of the LSPR position,  $\Delta\lambda_{\text{peak}}$ , for 25 °C <  $T$  < 200 °C (see Figures 2a), an irreversible blueshift for 200 °C <  $T$  < 600 °C (see Figures 2e,f,h,i), and an irreversible redshift for  $T$  > 600 °C (see Figures 2j,l);
- ii. A different change of the LSPR amplitude,  $\Delta A_{\text{peak}}$ , indicative of a different sensitivity of the LO- and TO-LSPR to hydrogen also depending on temperature;
- iii. A different shape of the kinetic profiles with the increase of temperature in Figures 2c,g,k indicative of different interactions of Ga with hydrogen and with a reaction rate increasing with temperature as detailed below.

The AFM images before and after hydrogen exposure, reported in the Supporting Information (see Figure S6, Supporting Information), show that the blueshift and change in the amplitude of LSPRs are not related to change of size and or morphology of the Ga NPs. Therefore, we discuss the different spectra variations and kinetic profiles in Figure 2 in terms of possible chemical reactions involving the H<sub>2</sub>-Ga NPs-Al<sub>2</sub>O<sub>3</sub> system, identifying three temperature regimes.

## 2.2. Hydrogen Sensing at 25 °C < $T$ < 200 °C

Figures 2a–c show the fully reversible change in the dielectric function of the LO mode at 3.5 eV upon exposure to H<sub>2</sub> in both spectroscopic mode (Figures 2a,b) (spectra plotted as a function of time of exposure to hydrogen) and kinetic mode (Figure 2c) (the maximum of LSPR peak is plotted versus time to better show the profile shape), with a blueshift  $\Delta\lambda_{\text{peak}}$  of  $\approx 22$  nm at saturation of Ga NP exposure to hydrogen, quickly reached after few seconds (<10 s depending on the H<sub>2</sub> pressure). Because of this complete reversibility and the solubility of H<sub>2</sub> into liquid Ga (see Table S1 in Section S10, Supporting Information), we

postulate that we are sensing the dissociative adsorption of hydrogen at surface sites and its interstitial diffusion in the liquid Ga NP as illustrated in Figure 2d according to:



The saturation level depends on the saturation of surface sites as well as on the solubility into the Ga NP. Several observations support this hypothesis: first, an Arrhenius plot, obtained by measuring the temperature-dependent initial rate of H<sub>2</sub> incorporation (as from profiles in Figure 2b), indicates a very low activation energy of  $E_a = 1.5$  meV for hydrogenation, suggesting physisorption and interstitial hydrogen storage into the NP without reactive steps. Interestingly, this determined 1.5 meV activation energy is two orders of magnitude lower than the activation energy for the thermal diffusion of hydrogen in Ga of 207 meV.<sup>[29]</sup> It is noteworthy that the 1.5 meV activation energy of adsorption/interstitial diffusion of hydrogen in liquid Ga NPs is also almost 3 order of magnitude lower than the activation energy of 800 meV for the adsorption of hydrogen on Pd NPs.<sup>[30]</sup> This decrease of order of magnitudes of the activation energy supports the plasmonic catalytic effect on the surface dissociative adsorption and interstitial diffusion of hydrogen according to the electromagnetic field maps of Figure 1. Second, we compared the Ga NPs–hydrogen kinetics with that observed when same Ga NPs were exposed to non-reactive He gas interstitially incorporated in Ga (see Section S6 and Figure S8, Supporting Information); here the observed slower kinetic of He diffusion, with atomic mass double that atomic-hydrogen, supports that atomic hydrogen is diffusing interstitially. Third, the spectra during the exposure to hydrogen (see Figure 2a) reveal a blueshift in the LSPR peak, which is indicative of electron accumulation (see further discussion below and additionally Section S1, Supporting Information), consistently with the donor character of metallic interstitial hydrogen. It is worth noting the timescale for the hydrogenation and dehydrogenation sensing showed in Figure 2c. Timescales for hydrogenation of 5–10 s and for full dehydrogenation of 100–200 s, depending on temperature and hydrogen pressure, have been measured. The quite fast response to hydrogenation is due to the liquid structure of Ga NP, with the shortest-neighbor Ga-Ga distance at 2.76 Å that can accommodate in the liquid easily interstitial hydrogen atoms (compare the higher diffusivity of hydrogen in liquid-Ga than in crystalline Pd as shown in Table S1 in Section S10, Supporting Information). It is noteworthy that Figure 2c shows that also after several cycles of exposure to hydrogen, the plasmon resonance peak returns reversibly to its original position and amplitude even at a modest temperature such as 25 °C, showing no hysteresis, oppositely to what has been reported for Pd/H<sub>2</sub> or MgH<sub>2</sub> NPs at  $T = 250$  °C.<sup>[31]</sup> More importantly, also the desorption kinetics does not slow down with cycling.

## 2.3. Hydrides Formation at 200 °C < $T$ < 600 °C

The non-reversible blueshift of both LO- and TO-LSPR (see Figures 2e,f) and the different kinetics observed at  $T$  > 200 °C

(Figure 2g) suggest a permanent modification that we associate with Ga-H hydrides formation reaction. In this case, the observed two-different slopes (e.g., the yellow and green shadowed areas in Figure 2g) kinetics correspond to (i) the initial rapid incorporation of interstitial hydrogen atoms in the liquid Ga NPs according to reactions (1–2) (yellow region in Figure 2g), followed by (ii) a slower kinetics (green region in Figure 2g), which we ascribe to reactive step of Ga–H bond formation as:



The strong change of the reaction rate with temperature for the hydride kinetics (green zone in Figure 2g), corresponding to an activation energy,  $E_a = 1.58 \pm 0.01$  eV, as obtained from an Arrhenius plot, supports that this is a reactive step that forms Ga–H bonds, whose chemical evidences have been obtained by XPS, Raman, and FTIR spectroscopies (see Section S4, Supporting Information). Interestingly, this activation energy compares well with the activation energies of bulk ( $162 \text{ kJ mol}^{-1} = 1.67$  eV) and nanocrystalline ( $144 \text{ kJ mol}^{-1} = 1.49$  eV)  $\text{MgH}_2$  formation.<sup>[32]</sup> As last step, the kinetic profiles also show that, when  $\text{H}_2$  exposure is terminated, the non-reacted hydrogen desorbes, and the profile is only partially recovered (red region in Figure 2b). This desorbed contribution decreases with the increase of temperature because more and more hydrogen is stored into the NPs with the increase of temperature. Several configurations of the Ga–H chemical bonding are possible, considering that Ga atoms prefer to form di-gallium hydrides<sup>[33]</sup> and that very recent theoretical studies of the hydride  $\text{GaH}_5\text{-P21/m}$  found that Ga atoms in the NPs may form wave-like chains and most of the  $\text{H}_2$  units are distributed around Ga chains.<sup>[34]</sup> Therefore, as illustrated in Figure 2d, two types of hydrogen species can exist in the Ga NP, that is, interstitial atomic hydrogen that can bind at single Ga sites and between Ga atoms of neighboring chains<sup>[35]</sup> forming Ga hydrides. The overall result is a permanent spectral blueshift of both the LO-SLPR and TO-LSPR plasmon resonances, as shown in Figure 2e,f. A free-electron Drude model is used to understand this blueshift by analyzing how the dielectric constant and plasmon resonance of liquid Ga NPs are modified by the change in the electron density due to the presence of hydrogen. We have performed electromagnetic simulations (see Experimental Section and Sections S1 and S2, Supporting Information) of a liquid Ga hemisphere-on-substrate geometry with a dielectric constant obtained from the Drude model as the free electron density is increased by a factor  $n$  with respect to the pristine (no hydrogen) Ga NPs. Figures 2h,i shows how the resonances blueshift and damp in agreement with the experimental results (Figure 2e,f,h,i), as the electron density in the particle increases, because of the donor character of hydrogen (see Section S1, Supporting Information for details). This indicates that the electron density in the Ga NPs increases<sup>[36]</sup> consistently with the electron donor character of interstitial hydrogen,<sup>[37]</sup> as well as with the formation of metallic  $\text{GaH}_5$  and/or  $\text{GaH}_3$  phases. The liquid Ga accommodates reversible plastic distortion and the hydrogenation process maintains the metallic character of the NP.<sup>[38]</sup> Consequently, both the LO-LSPR and TO-LSPR modes, are preserved.

Thus, the blueshift observed in the regime of sensing adsorption and of hydride formation supports that plasmonic Ga sensing and reaction to hydrogen is due to an electronic variation of the Ga NPs (as opposite to the usual redshift observed by plasmonic sensing of change in the refractive index of the surrounding media, for example, see Section S3 and Figure S2, Supporting Information).

The hypothesis that all these characteristics are enabled by the liquid Ga is supported by the electron microscopy study in Figure 3. We have previously demonstrated that those liquid Ga NPs on  $\text{Al}_2\text{O}_3$  have a solid  $\gamma\text{-Ga}$  core.<sup>[20]</sup> The HRETEM analysis in Figure 3d indicates that this solid core is not altered by the hydrogenation, supporting that liquid metal systems are a viable technology to sense faster and store more hydrogen. Specifically, at  $500^\circ\text{C}$  it has been estimated that the fraction of  $\text{H}_2$  in liquid Ga is  $\chi = \frac{2n_{\text{H}_2}}{n_{\text{Ga}}} = 8.7$  ( $n$  is the number of moles per cc),<sup>[39]</sup> which provides roughly 8–9 atoms of hydrogen per atom of Ga at atmospheric pressure of  $\text{H}_2$ , which is a very high solubility, likely due to the significant interstitial sites in a liquid metal.

#### 2.4. Interface Hydrogen Spillover and Reverse Oxygen Spillover at Plasmonic Hot-Spots at $T > 600^\circ\text{C}$

At  $T > 600^\circ\text{C}$ , Figures 2j–l (see also Figure S1b, Supporting Information) show that both the LO and TO-LSPR redshift and are irreversibly damped and a different kinetics is also recorded, indicating a different interaction occurring with hydrogen, which has been revealed by transmission electron microscopy (TEM). Figures 3a,b show the STEM-EDS (scanning transmission electron microscopy-energy dispersive spectroscopy) images of the Ga NPs before and after the exposure to hydrogen. Upon exposure to hydrogen and broadband illumination, major modifications are seen at the Ga NP/sapphire interface that is no longer sharp. The elemental chemical maps and d-spacing analysis indicated the formation of interfacial  $\text{Ga}_2\text{O}_3$  at locations that coincide with the field intensity hot spots of the LO-LSPR, suggesting that the LO-LSPR, which confine the electromagnetic field in an extended region of the NP-substrate interface, catalyzes a Ga/ $\text{Al}_2\text{O}_3$  modification mediated by hydrogen. Interestingly, we have conducted experiments where the sample was exposed to hydrogen at  $600^\circ\text{C}$  and irradiated with a 375 nm blue laser to excite only the TO mode; the analysis of those samples did not reveal any  $\text{Ga}_2\text{O}_3$  at the interface, supporting our finding that it is the LO mode hot spots activating the spillover. Furthermore, these STEM images provide a direct visualization of the reverse-oxygen spillover effect from the  $\text{Al}_2\text{O}_3$  support to a NP due the simultaneous presence of hydrogen and resonant illumination of the Ga NP LSPR which activates a hydrogen mediated displacement of oxygen atoms from  $\text{Al}_2\text{O}_3$  to Ga at interfaces as described below. Remarkably, the reverse-oxygen spillover leading to the interfacial  $\text{Ga}_2\text{O}_3$  requires simultaneously hydrogen and an electromagnetic confinement at the interface Ga NP/ $\text{Al}_2\text{O}_3$ . Our previous study<sup>[20]</sup> demonstrated that in absence of hydrogen Ga NPs are stable on  $\text{Al}_2\text{O}_3$  at temperatures above  $600^\circ\text{C}$ ; hence, the observed spillover is not due to a thermal activated reaction; similarly, we did not observe the same interface reactivity when

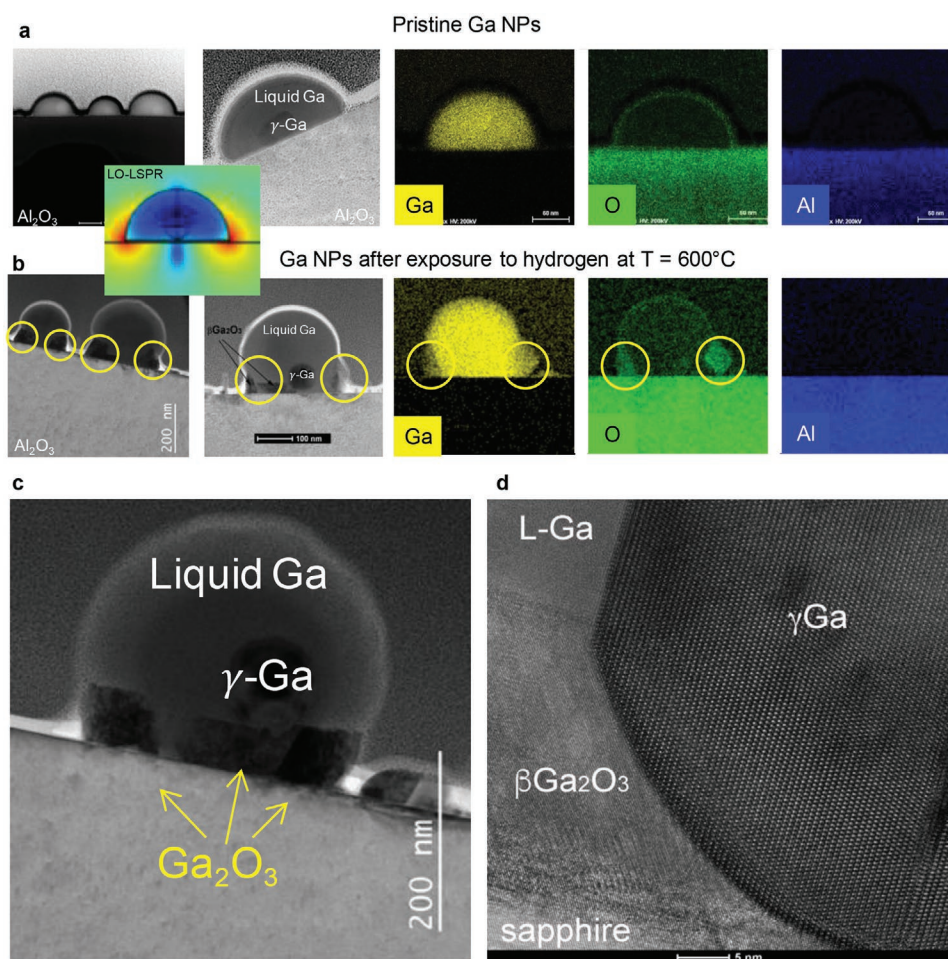
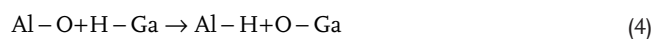


**Figure 3.** HAADF-STEM images and STEM-EDS elemental maps of Ga NPs supported on  $\alpha$ - $\text{Al}_2\text{O}_3$  before (a) and after (b) the interaction with hydrogen at  $T = 600^\circ\text{C}$  and 1 Torr according to the kinetics in Figure 2j,k. The elemental maps of Ga (yellow), O (green), and Al (blue) show the reverse spillover of oxygen into the Ga NP, while there is no interdiffusion of Ga and Al. The scale bar in the chemical maps is 50 nm. The inset shows the longitudinal LO-LSPR hot spots localized at the interface between the Ga NPs and the  $\text{Al}_2\text{O}_3$  support. c) TEM image of the Ga/ $\alpha$ - $\text{Al}_2\text{O}_3$  interface modifications upon hydrogen interaction, that is, the formation of  $\text{Ga}_2\text{O}_3$  localized at the interface. The yellow circles highlight the spots of formation of the  $\text{Ga}_2\text{O}_3$  by the spillover reaction. d) High-resolution TEM image of the new phase  $\beta$ - $\text{Ga}_2\text{O}_3$  formed at the interface of the liquid Ga NPs and the sapphire. The image shows the  $\gamma$ -Ga solid core of the Ga NPs is not altered by hydrogenation. The correlation between the location where  $\text{Ga}_2\text{O}_3$  formed and the regions of highest Ga LSPR field enhancement can be seen in electromagnetic near-field enhancement maps, showing the Ga NPs/ $\text{Al}_2\text{O}_3$  interface modifications occurred at hot-spots.

a thin continuous layer of Ga (no plasmon resonance observed) is deposited on  $\text{Al}_2\text{O}_3$  and exposed to hydrogen. Therefore, the observed phenomenon is an inherently plasmonic photocatalytic nanoscale activity of Ga NP/ $\text{Al}_2\text{O}_3$  that synergistically and simultaneously produces hydrogen spillover<sup>[40]</sup> and reverse-oxygen spillover, which can be schematized as:



The interfacial formation of  $\text{Ga}_2\text{O}_3$  is responsible for the red-shift of the plasmon resonances in Figure 2j, as consistently supported by the electromagnetic simulations (see Figure 2l) where both the refractive index of the substrate and the electron density inside the particle both increase (see Section S2, Supporting Information). By increasing the refractive index of the substrate, we mimic the effect produced by the formation of the  $\text{Ga}_2\text{O}_3$  layer at the NP-substrate interface (Figure 3i). Because

the refractive index of  $\text{Ga}_2\text{O}_3$  ( $n \approx 1.9$ ) is higher than that of the substrate ( $n \approx 1.78$ ), we have considered an effective substrate with a refractive index between those two values. In order to include other surface oxidation effects, we have considered the Ga hemisphere to be embedded in a medium of an effective refractive index slightly larger than 1 ( $\approx 1.1$ ).

The fact that NPs can catalytically boost oxygen transfer from the support to the NP was also reported for Pt NPs on ceria ( $\text{CeO}_2$ ).<sup>[26]</sup> The driving force for this plasmon catalyzed hydrogen and oxygen spillover is the energy for the interfacial reactivity involving both hydrogen and gallium at the Al and O sites of the  $\text{Al}_2\text{O}_3$  support, further detailed in Supporting Information (see Section S7, Supporting Information). Interestingly at temperatures near  $600^\circ\text{C}$ , a steady state condition between the hydrogenated metallic Ga NPs and the oxidized interface is reached. Even for prolonged exposure to hydrogen at  $600^\circ\text{C}$ , a minimum in the LSPR is reached but never completely quenched,



indicating that the oxidation of the Ga NPs from the reverse oxygen spillover is limited to the interface, and the entire Ga NP is not completely transformed to  $\text{Ga}_2\text{O}_3$ . Measurements from the TEM images indicate that this steady state condition, representing the maximum spillover oxygen capacity, represents a 15–20% of the Ga NP volume. This steady state can be explained considering that  $\text{Ga}_2\text{O}_3$  domains once formed at the interface are also catalytically reduced by the hydrogen into the NPs. Another interesting feature revealed by the high-resolution transmission electron microscopy (HRTEM) analysis is that the solid  $\gamma$ -Ga lattice core present in the liquid NPs is not altered by hydrogen, supporting the hypothesis that hydrogen solubilizes and reacts in liquid Ga but not in a highly ordered Ga crystal lattice.

This steady-state condition is stable over years (as shown in the Section S5, Supporting Information). Those Ga NPs exposed to hydrogen at 600 °C have been re-measured after 2 years of air exposure in the lab. Both TEM and LSPR showed good stability, indicating excellent resilience to aging and the opportunity for reusing those Ga NPs in hydrogen catalytic reactions up to 600 °C.<sup>[41]</sup>

## 2.5. Site-Selectivity and Sensitivity of Hot-Spot-Driven Interaction

The experimental as well as simulated spectra in Figures 2e,h highlight also a different sensitivity of the LO-LSPR and TO-LSPR to the various regimes of interaction with hydrogen, indicating a different role of the LO and TO modes in catalyzing the various chemical reactions involving hydrogen uptake and sensing, hydrogen spillover, and reverse-oxygen spillover. Specifically, the TO-LSPR hot-spots, with electromagnetic confinement mainly at the NPs surface, drive dissociative hydrogen adsorption/solubility forming hydrides. The LO-LSPR, with hot-spots more localized at the interface with the  $\text{Al}_2\text{O}_3$  support (see Figure 1f), is purely dipolar and the electronic plasma oscillates with the largest amplitude corresponding to the Ga NP diameter parallel to the substrate surface and activates heterogeneous reactions of hydrogen spillover from Ga NPs into  $\alpha$ - $\text{Al}_2\text{O}_3$  and reverse-oxygen spillover from  $\alpha$ - $\text{Al}_2\text{O}_3$  to Ga NP. Note that HRTEM in Figure 3 does not show any propagation of the new  $\text{Ga}_2\text{O}_3$  phase toward the Ga NP surface where the TO electromagnetic field applies, indicating that spillover reactions is not driven by TO-modes. This plasmon mode catalysis specificity has never been achieved before. Therefore, plasmons can not only catalyze reactions but enable site-selectivity through their localized strong electromagnetic fields at hot-spots.

In order to address the sensitivity of the Ga NPs sensor to the various hydrogen related processes there are several factors to be considered, that is:

- The shift in the LSPR wavelength,  $\Delta\lambda_{\text{peak}}$ ;
- The size of Ga NPs, which also dictates the LSPR wavelength  $\lambda_{\text{peak}}$ ; the spectral position is also dependent on the NPs radius, and hence, volume and surface, and generally longer wavelengths are also associated to the redshift of the LSPR by the increase in the NP size;
- The different distribution of the electromagnetic field for the LO and TO resonant modes.

By the analysis of the variation of the LO and TO modes at the same photon energy/(wavelength) of 3.55 eV it is possible to establish whether the obtained  $\Delta\lambda_{\text{peak}}$  depends on the amount of absorbed hydrogen atoms (in this case, a larger particle volume should yield a larger  $\Delta\lambda_{\text{peak}}$ ) or if it is dictated by the spectral position of the LSPR and by the LO versus TO enhancement maps. Similarly, the comparative analysis of the LO modes at 1.05 eV for the larger NPs and at 3.5 eV for the smaller NPs, allows to discern the effect on sensitivity of  $\lambda_{\text{peak}}$ ,  $\Delta\lambda_{\text{peak}}$ , and size.

Focusing on the blueshift of LSPR observed at  $T < 600$  °C for hydrogen sensing and storage as hydrides and interstitial hydrogen, the  $\Delta\lambda_{\text{blue}}$  is approximately the same for both the TO-LSPR at 3.55 eV and LO-LSPR at 3.55 eV (i.e., 22–23 nm), and very similar to the shift of 24 nm for the LO-LSPR at 1.05 eV; hence, the sensitivity, in terms of  $\Delta\lambda$ , of an electron transfer-based Ga NP plasmonic hydrogen sensor is not dictated by the spectral position of LSPR, differently from refractive index Pd-based systems. On the other hand, the amplitude changes significantly, and by plotting the rate of variation of the amplitude of the LSPR upon exposure to hydrogen (see Figure 4b) we found that the sensitivity of TO-LSPR is higher than LO-LSPR. This is consistent with the theoretical results shown in Figure 2i, in which the amplitude of the LO changes less than the amplitude of the TO mode for equal increase of the electron density in the NP. This can be explained considering that for the TO mode, although the dipolar contribution dominates, other modes of higher order start to contribute, in such a way that hot-spots appear also at the Ga NP surface. As a result, and as shown by Figure 1e, for those NPs showing both LO and TO modes, the average of the electromagnetic field enhancement over the surface of the NP, is higher for the TO mode.

This dependence on the electromagnetic fields together with the fact that the  $\Delta A$  is also almost independent on temperature (the temperature was intentionally changed to see if there was a change in the reversible kinetics) supports an electromagnetic plasmonic-driven surface sensing and not a thermal activated adsorption/diffusion based mechanism.

The plasmonic effect has further been proven also by investigating the wavelength dependence of the photocatalytic rate measured at room temperature as shown in Figure 4a. Combinations of filters were placed in the beam path to excite at various photon energies close and far from the LSPR peak. It is noteworthy that the adsorption and hydride formation rates are maximum at the LSPR energy, indicating that they are plasmonically enhanced.

The role of the plasmonic enhancement depending also on the different resonance mode is also demonstrated in Figure 4c which compares the adsorption/solubilization and desorption of the LO- and TO-LSPR both at 3.55 eV (hence independently of the sampling energy/wavelength). The TO-LSPR results in an adsorption/solubilization kinetic faster (<5 s) than the LO-LSPR, confirming that the electromagnetic field of the TO-LSPR drives the hydrogen adsorption and interstitial accumulation. This hypothesis is also corroborated by electromagnetic simulations shown in Figure 1e, which plots the spectral dependence of the near-field enhancement averaged over the NP's surface  $\langle |E|^2 \rangle$ . Increasing the NP size, the values of  $\langle |E|^2 \rangle$  are higher for



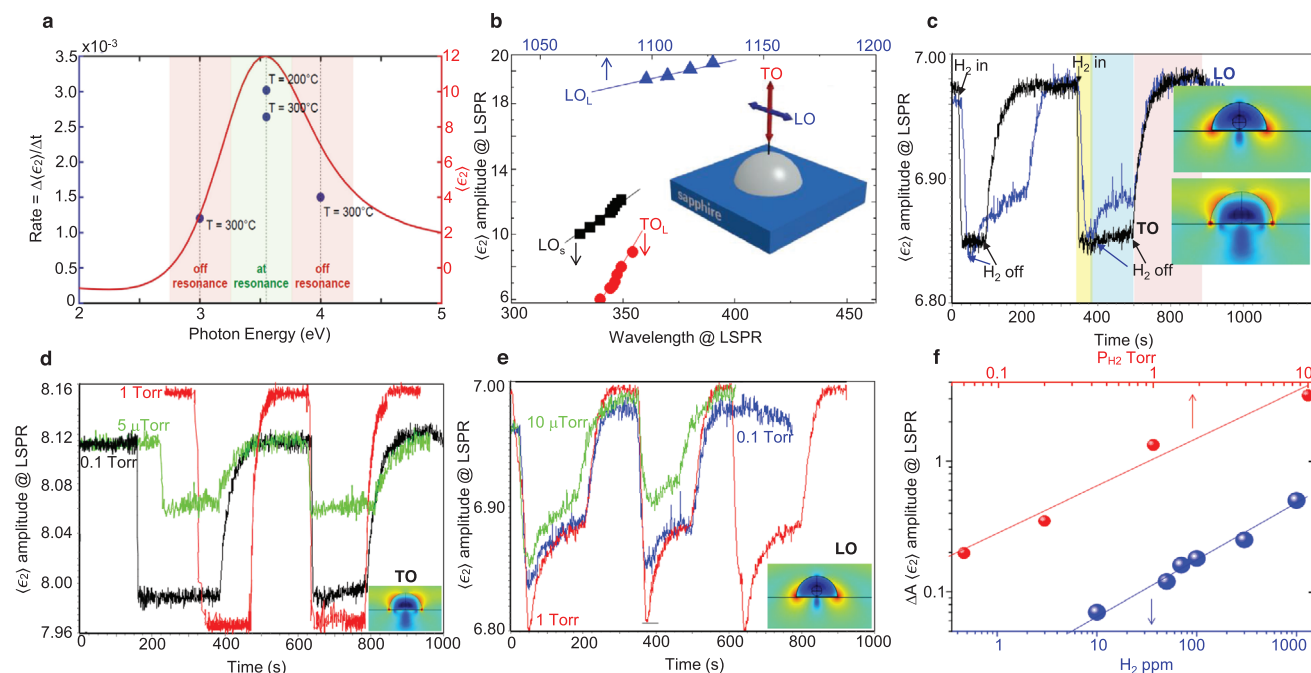


**Figure 4.** Hot-spot-driven selectivity and sensitivity of the Ga nanoantennas. a) Wavelength dependence of the rate of hydrides formation. b) Amplitude versus wavelength of the LO- and TO-LSPR for both smaller (diameter of 85 nm) and larger (diameter of 260 nm) Ga NPs during exposure to hydrogen at 300 °C and 1 Torr. c) Comparison of the kinetics of the LO-LSPR and TO-LSPR, both at the energy of 3.55 eV at 100 °C and 0.1 Torr of hydrogen. The inset reminds where the hot spots are localized for the two plasmon modes. d) Kinetic profiles of the TO-LSPR at different pressures of hydrogen and at  $T = 100$  °C. e) Kinetic profiles of the LO-LSPR at different pressures of hydrogen and at  $T = 100$  °C. f) Sensitivity of the hydrogen sensing in terms of variation of the amplitude of the plasmon resonance in mixtures of  $H_2/Ar$ . Data in (a) have been acquired using filters to illuminate NPs with selected wavelengths, while all the other data are acquired under broadband illumination from a Xe lamp.

the TO mode than the LO-mode, together with an increase of the surface spatial near-field distribution maps of the TO mode, yielding a higher probability of  $H_2$  molecule to interact with the NP LSPR. Interestingly, the desorption kinetics is monotone for the TO-LSPR, while for the LO-LSPR shows a double step desorption with the part being similar to the TO-kinetics, while the first desorption step considering the hot-spots at the interface with the substrate, we can infer it represents the desorption of hydrogen localized at the interface with the support where hydrogen could also be trapped into spillover according to reaction (4).

This implies, in terms of design of the Ga NPs, that to have the TO-LSPR in the measurable spectral range of our spectroscopic ellipsometer peaked at  $<6$  eV, Ga NPs with a radius  $>60$  nm should be preferred. For response time  $<10$ – $20$  s any radius of Ga NPs can exploit both the TO and the LO-LSPR.

The isothermal adsorption of  $H_2$  at room temperature at different hydrogen pressures has also been investigated by exposing them to pulses of gradually decreasing  $H_2$  pressure in vacuum as shown in Figure 4d for both the LO- and TO-LSPR of particles that also have different size. Interestingly, the rate of the adsorption is almost pressure independent, supporting a mainly plasmon catalyzed sensing process. On the other hand, a pressure-dependent adsorption/solubilization plateau level is reached for the TO-LSPR (see Figures 4c,d), indicating that at  $T < 200$  °C (in absence of any reactive step to

hydrides) the sensing is controlled by the maximum number of available surface sites for adsorption, which are quickly saturated aided by the TO electromagnetic enhancement confined at the NP surface and by the pressure related solubility of hydrogen into the Ga NPs. We also used the TO LSPR to derive the LoD (Limit of Detection) of the plasmonic Ga NPs sensors by exposing them to pulses of different hydrogen pressures from 10 Torr to 50  $\mu$ Torr and by measuring the amplitude variation as shown in Figure 4f,e. We extrapolate that the LoD is  $<5$   $H_2$   $\mu$ bar as shown in Figure 4f, and considering that the level of noise in the  $\Delta A$  signal is 0.01 a discernible signal can be extrapolated for a  $H_2$  pressure of 100 nTorr (see Figure S11, Supporting Information and corresponding discussion in Section S9, Supporting Information). In order to better assess the sensitivity, we also tested sensing  $H_2$  in more realistic conditions of flowing  $Ar/H_2$  mixtures changing the relative pressure of  $H_2$  as shown in Figure 4f, and a LoD of 5 ppm can be extrapolated, which is one of the lowest LoD to  $H_2$  reported so far. The other interesting features to consider are the fast sensor to hydrogen in a broad temperature range can be reversibly used without damage of the sensor; the stability and the resistance to poisoning by oxidation, because even if the Ga NPs in presence of air could form a thin  $\approx 1$  nm surface oxide shell, when exposed to hydrogen it is quickly reduced and its performance re-established (see Section S8, Supporting Information).

### 3. Conclusions

Although it is often assumed that new chemical phenomena may appear in nanostructured materials, there are only a few examples in which such effects have been clearly identified at the atomic scale. Here we have first provided evidences of multiple processes occurring in a plasmonic Ga nanoantenna supported on  $\text{Al}_2\text{O}_3$  interacting with hydrogen, such as interstitial metallic hydrogen incorporation, hydrides formation, hydrogen spillover, and reverse-oxygen spillover. First, at temperatures from room temperature to 200 °C, a purely electronic effect involving electron transfer from hydrogen to Ga NPs, resulting in interstitial metallic hydrogen makes the system advantageous as rapid ( $\approx 5$  s) and reusable optical  $\text{H}_2$  sensors because of the full reversibility and stability of the system. A second channel involves hydrogen storage by the direct photocatalyzed hydrogen dissociation and Ga–H bond formation, yielding hydrides with large deviations from ideal stoichiometry that can exist as multiphase systems. A third reactive interface channel occurring only at temperature higher than 600 °C involves reverse spillover of oxygen from  $\text{Al}_2\text{O}_3$  to Ga, with concomitant hydrogen storage by way of the spillover reaction at the interface with  $\text{Al}_2\text{O}_3$  activated by the in-plane plasmon resonance (longitudinal plasmon mode). Most importantly, we demonstrate the site-selectivity of those reactions driven by the longitudinal and transverse plasmon resonance of non-spherical NPs. From the technological point of view of a hydrogen sensing and storage material, plasmonic Ga NPs/ $\text{Al}_2\text{O}_3$  possess many compelling properties, including: (i) accommodating good volumetric and gravimetric densities of hydrogen; considering the possible metallic phase  $\text{GaH}_3$  with interstitial molecular  $\text{H}_2$  and H-atoms, a high hydrogen storage capacity in the Ga NP estimated as of 8.7 H-atoms per Ga atom; (ii) exhibiting rapid adsorption kinetics; (iii) demonstrating easy activation; (iv) providing low temperature dissociation and desorption; (v) ensuring long-term cycling stability; (vi) exhibiting high reversibility; (vii) providing a photocatalytic system that is stable up to temperature of 600 °C. Therefore, a new plasmon-photocatalytic system Ga/ $\text{Al}_2\text{O}_3$  reversibly operating and responding to hydrogen up to 600 °C is demonstrated, with characteristics that overcome common catalytic limitations and suggest a promising role for the remarkable properties of multiphase supported Ga NPs in a future hydrogen-based economy.

### 4. Experimental Section

**Preparation of Ga NPs:** A reproducible plasmonic response that can be simply tailored by the NPs size and Ga fluxing time was achieved by a one-step deposition of Ga NPs at room temperature in a Veeco GEN II molecular beam epitaxial system under ultrahigh vacuum conditions<sup>[20]</sup> without any nanolithography process. The base vacuum pressure of the system was  $10^{-11}$  Torr before starting the Ga flux indicating that the presence of impurities can be excluded. The fluxing Ga time was used to control the NP size. The  $\alpha\text{-Al}_2\text{O}_3$  (0001) support was preliminarily degassed at 200 °C for 1 h in the pre-chamber to remove any residual contamination from its surface. The MBE system was equipped with an in situ spectroscopic ellipsometer (UVISEL, HORIBA) that was used to acquire spectra of the pseudodielectric function during the Ga deposition to monitor the plasmon resonance peaks position and set the deposition time and LSPR energies.<sup>[20]</sup>

**Interaction of Ga NPs with Hydrogen:** The interaction of Ga NPs supported on  $\text{Al}_2\text{O}_3$  with hydrogen involved exposure of the samples to hydrogen in flow mode (500 sccm), at various  $\text{H}_2$  pressures in the range 0–10 Torr and at temperatures in the range 25–600 °C. The interaction with hydrogen was also monitored in real-time with an in situ spectroscopic ellipsometer.

**Characterization:** TEM cross-sectional samples were prepared by the FEI Nova dual beam FIB system. HRTEM and HAADF-STEM (high angle annular dark field STEM) imaging, selected-area electron diffraction, and chemical composition analysis by STEM-EDS had been carried out using a Titan G2 80–200 TEM/STEM with ChemiSTEM technology.

Atomic force microscopy was used to map sample topography with an Autoprobe CP-VEECO in a single-pass mode using gold-coated Si tips (the frequency was 80 Hz) in non-contact mode.

In situ spectroscopic ellipsometry<sup>[42]</sup> was used to monitor in real time the kinetics of interaction with  $\text{H}_2$  recording the variation of the plasmonic response of the ensemble of Ga NPs by recording spectra of the pseudodielectric function,  $\langle\epsilon\rangle = \langle\epsilon_1\rangle + i\langle\epsilon_2\rangle$  showing the plasmon resonances. Ellipsometric spectra were acquired using a phase-modulated spectroscopic ellipsometer (UVISEL, Horiba) in the 0.75–6.5 eV spectral range with 0.01 eV resolution, every 1 s. The ellipsometer was assembled on the reactor at an angle of incidence of 70°. An ellipsometer was assembled in situ on the MBE reactor monitoring the growth of the Ga NPs and the evolving plasmon resonances. Before taking the sample out of the MBE, the in situ spectrum was acquired at a pressure of  $10^{-10}$  Torr, giving the signature of the plasmon resonance of bare and cleaned Ga NPs before any possible oxidation by air exposure. Then the samples were characterized ex situ and transferred to another reactor for the hydrogen treatment.

Also, the hydrogen reactor had the ellipsometer assembled in situ to monitor in real time the kinetics of processes of interaction with hydrogen. Before initiating the hydrogen, the spectrum consistently with TEM revealed the  $<1$  nm  $\text{Ga}_2\text{O}_3$  shell formed by air oxidation; therefore, this oxide shell was removed first (see Section S8, Supporting Information) and the authors made sure by checking and comparing the ellipsometric spectra that they got back to the condition of bare/cleaned (no oxygen around) Ga NPs before starting investigating the interaction with hydrogen.

All of the kinetic measurements were done under broadband illumination. Furthermore, to demonstrate that the authors were in presence of a plasmon catalytic effect, measurements reported in Figure 4a were also made with intentionally irradiating at the LO and TO plasmon maximum using filters.

**Optical and Electromagnetic Simulation:** Finite-difference time-domain (FDTD) calculations were performed to simulate a hemisphere-on-substrate geometry. The FDTD method allowed the Maxwell's equations to be solved for an arbitrary geometry. In this study, the software FDTD solutions Version 8.16 from Lumerical Inc. was employed. Total-field/scattered field light source conditions were used in all simulations. An illuminating linearly polarized plane-wave was set to propagate perpendicular to the substrate. The wavelength spectral range analyzed was from 200 to 1500 nm to mimic experimental conditions. A non-uniform mesh was used in the simulation region. A finer mesh was defined in the vicinity of the NP. In this region, the mesh step was fixed to  $d_x = d_y = d_z = 1$  nm. The absorption cross-section was calculated within the total-field/scattered-field formalism. The near field maps were obtained through a frequency-domain field and power monitor containing the propagation and polarization directions. The incident electromagnetic wave was set to have an intensity of  $|E_0|^2 = 1$ .

Finite element method (FEM) calculations implemented using COMSOL Multiphysics 5.2 (Burlington, MA, USA) were also performed to simulate a hemisphere-on-substrate geometry. In particular, the wave optics module was used that allowed the differential form of Maxwell's equations (in the frequency domain) together with the initial and boundary conditions to be formulated and solved. The equations were solved using the FEM with numerically stable edge element discretization in combination with state-of-the-art algorithms for preconditioning and solution of the resulting sparse equation systems.

In this particular case, the problem was solved in two steps: first it was computed a background field from the plane wave incident on the substrate, and then the uses that to arrive at the total field with the NP present. The wavelength spectral range analyzed was from 200 to 800 nm to mimic experimental conditions. A finer mesh was defined in the vicinity of the NP. In this region, a tetrahedral mesh with maximum size of 8 nm was used.

## Supporting Information

Supporting Information is available from the Wiley Online Library or from the author.

## Acknowledgements

The authors thank all of the students and colleagues in their groups who were actively involved with nanoparticles research. M.L., Y.G., and F.M. have received funding from the European Union's Horizon 2020 Research and Innovation Program under Grant Agreement No. 899598—PHEMTRONICS. F.M. acknowledges MINECO (Spanish Ministry of Economy and Competitiveness, project PGC2018-096649-B-I00).

## Conflict of Interest

The authors declare no conflict of interest.

## Data Availability Statement

Research data are not shared.

## Keywords

gallium, hydrogen storage, metal hydrides, optical hydrogen sensing, oxygen reverse spillover, photocatalysis, plasmonics

Received: January 19, 2021

Revised: April 3, 2021

Published online: June 2, 2021

- [1] Multi-Year Research, *Development, and Demonstration Plan, 2011–2020. Section 3.7 Hydrogen Safety, Codes and Standards*, U.S. Department of Energy, Fuel Cell Technologies Office, **2015**, available at [https://www.energy.gov/sites/default/files/2015/06/f23/fcto\\_myrrdd\\_safety\\_codes.pdf](https://www.energy.gov/sites/default/files/2015/06/f23/fcto_myrrdd_safety_codes.pdf).
- [2] S. Linic, U. Aslam, C. Boerigter, M. Morabito, *Nat. Mater.* **2015**, *14*, 567.
- [3] N. Taccardi, M. Grabau, J. Debuschewitz, M. Distaso, M. Brandl, R. Hock, F. Maier, C. Papp, J. Erhard, C. Neiss, W. Peukert, A. Görling, H.-P. Steinrück, P. Wasserscheid, *Nat. Chem.* **2017**, *9*, 862.
- [4] M. Vadai, D. K. Angell, F. Hayee, K. Sytwu, J. A. Dionne, *Nat. Commun.* **2018**, *9*, 4658.
- [5] N. Fukuoka, K. Tanabe, *J. Appl. Phys.* **2019**, *126*, 023102.
- [6] N. Fukuoka, K. Tanabe, *Nanomaterials* **2019**, *9*, 1235.
- [7] T. C. Narayan, F. Hayee, A. Baldi, A. Leen Koh, R. Sinclair, J. A. Dionne, *Nat. Commun.* **2017**, *8*, 14020.
- [8] F. Sterl, N. Strohfeldt, S. Both, E. Herkert, T. Weiss, H. Giessen, *ACS Sens.* **2020**, *5*, 917.
- [9] N. Liu, M. L. Tang, M. Hentschel, H. Giessen, A. P. Alivisatos, *Nat. Mater.* **2011**, *10*, 631.
- [10] S. Mukherjee, L. Zhou, A. M. Goodman, N. Large, C. Ayala-Orozco, Y. Zhang, P. Nordlander, N. J. Halas, *J. Am. Chem. Soc.* **2014**, *136*, 64.
- [11] D. Sil, K. D. Gilroy, A. Niaux, A. Boulesbaa, S. Neretina, E. Borguet, *ACS Nano* **2014**, *8*, 7755.
- [12] L. Zhou, C. Zhang, M. J. McClain, A. Manjavacas, C. M. Krauter, S. Tian, F. Berg, H. O. Everitt, E. A. Carter, P. Nordlander, N. J. Halas, *Nano Lett.* **2016**, *16*, 1478.
- [13] W. Liu, K.-F. Aguey-Zinsou, *J. Mater. Chem. A* **2014**, *2*, 9718.
- [14] H. Gasan, N. Aydinbeyli, O. N. Celik, Y. M. Yaman, *J. Alloys Compd.* **2009**, *487*, 724.
- [15] Y. Gutiérrez, M. M. Giangregorio, F. Palumbo, A. S. Brown, F. Moreno, M. Losurdo, *Opt. Express* **2019**, *27*, A197.
- [16] C. Langhammer, Z. Yuan, I. Zorić, B. Kasemo, *Nano Lett.* **2006**, *6*, 833.
- [17] J. Gaetz, J. J. Reilly, V. A. Yartys, J. P. Maehlen, B. M. Bulychev, V. E. Antonov, B. P. Tarasov, I. E. Gabis, *J. Alloys Compd.* **2011**, *509*, S517.
- [18] S. Yue, Y. Hou, R. Wang, S. Liu, M. Li, Z. Zhang, M. Hou, Y. Wang, Z. Zhang, *Opt. Express* **2019**, *27*, 19331.
- [19] C. Wadell, F. A. A. Nugroho, E. Lidström, B. Iandolo, J. B. Wagner, C. Langhammer, *Nano Lett.* **2015**, *15*, 3563.
- [20] M. Losurdo, A. Suvorova, S. Rubanov, K. Hingerl, A. S. Brown, *Nat. Mater.* **2016**, *15*, 995.
- [21] P. C. Wu, M. Losurdo, T.-H. Kim, S. Choi, G. Bruno, A. S. Brown, *J. Vac. Sci. Technol., B: Microelectron. Nanometer Struct.–Process., Meas., Phenom.* **2007**, *25*, 1019.
- [22] Y. Gutiérrez, M. Losurdo, P. García-Fernández, M. Sainz de la Maza, F. González, A. S. Brown, H. O. Everitt, J. Junquera, F. Moreno, *Adv. Opt. Mater.* **2019**, *7*, 1900307.
- [23] P.-S. Yen, N. D. Deveau, R. Datta, *AIChE J.* **2017**, *63*, 1483.
- [24] D. C. Camacho-Mojica, B. Cunnig, S. Chatterjee, S. Jin, F. Ding, J.-C. Charlier, R. S. Ruoff, *J. Phys. Chem. C* **2019**, *123*, 26769.
- [25] C. Tang, J. Kang, Z. Zhang, J. Zou, X. He, Y. Xu, *Int. J. Hydrogen Energy* **2015**, *40*, 16278.
- [26] G. N. Vayssilov, Y. Lykhach, A. Migani, T. Staudt, G. P. Petrova, N. Tsud, T. Skála, A. Bruix, F. Illas, K. C. Prince, V. Matolín, K. M. Neyman, J. Libuda, *Nat. Mater.* **2011**, *10*, 310.
- [27] M. W. Knight, T. Coenen, Y. Yang, B. J. M. Brenny, M. Losurdo, A. S. Brown, H. O. Everitt, A. Polman, *ACS Nano* **2015**, *9*, 2049.
- [28] B. Spackova, P. Wrobel, M. Bockova, J. Homola, *Proc. IEEE* **2016**, *104*, 2380.
- [29] P.-S. Yen, N. D. Deveau, R. Datta, *Ind. Eng. Chem. Res.* **2018**, *57*, 1607.
- [30] F. A. A. Nugroho, I. Darmadi, L. Cusinato, A. Susarrey-Arce, H. Schreuders, L. J. Bannenber, A. B. da Silva Fanta, S. Kadkhodazadeh, J. B. Wagner, T. J. Antosiewicz, A. Hellman, V. P. Zhdanov, B. Dam, C. Langhammer, *Nat. Mater.* **2019**, *18*, 489.
- [31] C. Zlotea, Y. Oumellal, S.-J. Hwang, C. M. Ghimbeu, P. E. de Jongh, M. Latroche, *J. Phys. Chem. C* **2015**, *119*, 18091.
- [32] B. D. Adams, A. Chen, *Mater. Today* **2011**, *14*, 282.
- [33] A. Köhn, H.-J. Himmel, B. Gaertner, *Chem. - Eur. J.* **2003**, *9*, 3909.
- [34] Y.-L. Ning, W.-H. Yang, Q.-J. Zang, W.-C. Lu, *Phys. B* **2017**, *525*, 36.
- [35] J. Ångström, R. Johansson, T. Sarkar, M. H. Sørby, C. Zlotea, M. S. Andersson, P. Nordblad, R. H. Scheicher, U. Häussermann, M. Sahlberg, *Inorg. Chem.* **2016**, *55*, 345.
- [36] D. J. Henry, *J. Phys. Chem. C* **2013**, *117*, 26269.



- [37] B. G. Ershov, E. V. Abkhalimov, R. D. Solovov, V. I. Roldughin, *Phys. Chem. Chem. Phys.* **2016**, *18*, 13459.
- [38] K. Yvon, Z. Kristallogr.- Cryst. Mater. **2003**, *218*, 108.
- [39] R. Datta, Y. H. Ma, P.-S. Yen, N. Deveau, I. Fishtik, I. Mardilovich, *Supported Molten Metal Membranes for Hydrogen Separation*, Technical Report, Worcester Polytechnic Inst., Worcester, MA, USA **2013**, available at <https://doi.org/10.2172/1123819>.
- [40] J. Im, H. Shin, H. Jang, H. Kim, M. Choi, *Nat. Commun.* **2014**, *5*, 3370.
- [41] During the revision of the manuscript, after 8 months from the original data acquisition, experiments were repeated on the same samples as in Figure 2, stored at ambient conditions in the lab, under the same hydrogen conditions, and the same phenomena occurred again demonstrating the stability and possibility to reuse NPs.
- [42] M. Losurdo, K. Hingerl, *Ellipsometry at the Nanoscale*, Springer, Berlin, Germany **2013**.